Applied Physics A (2022) 128:965
https://doi.org/10.1007/s00339-022-06028-4

Applied Physics A
Materials Science & Processing

Hidden impurities in transparent conducting oxides: study of vacancies-related defects and impurities in (Cu–Ni) co-doped ZnO films

Qais M. Al-Bataineh[1,2,3] · Ahmad A. Ahmad[2] · Ihsan A. Aljarrah[2] · Ahmad M. Alsaad[2] · Ahmad Telfah[1,4]

Received: 9 June 2022 / Accepted: 4 September 2022 / Published online: 11 October 2022

Abstract
The effect of hydrogen and nitrogen impurities on the physical properties of transparent conductive oxides is investigated in this study. Therefore, 5 wt.% of copper and 5 wt.% of nickel co-doped zinc oxide ((Cu–Ni)/ZnO) films were prepared using the sol–gel method. The (Cu–Ni)/ZnO films were annealed in an oven at 500 °C for 2 h under air, vacuum, nitrogen, and argon atmospheres. The synthesized zinc hydroxide film was transformed to zinc oxide film during the annealing by evaporating H_2O. Films annealed under the mentioned atmosphere including as-prepared one were characterized by analyzing with UV–Vis and FTIR spectra in addition to the 2D mapping electrical conductivity of the surface measured by the 4-point probe. The annealed films under air, vacuum, and argon atmospheres led to generate H-related impurities bounded to the oxygen vacancy (H_O) which they act as shallow donor defects resulting in forming (Cu–Ni)/ZnO films into n-type materials. Whereas, the film annealed under a nitrogen atmosphere has N-related defects bounding to the zinc vacancy (N_{Zn}) which they act as shallow acceptor defects resulting in transforming the film from n-type to p-type. These defects affect the optical, electrical, and optoelectronic properties of the (Cu–Ni)/ZnO films.

Keywords Transparent conductive oxides (TCOs) · Zinc oxide (ZnO) · Shallow donor defects · Shallow acceptor defects · Oxygen vacancy · Zinc vacancy · Optical and optoelectronic properties · Electrical conductivity

1 Introduction

Transparent conducting oxides (TCOs) are broadly used in electronic and optoelectronic devices, sensors, memories, batteries, and transistors due to their intriguing physical properties [1]. The n-type TCOs, zinc oxide (ZnO) in particular, have acquired much attention due to their physical properties, such as considerable bandgap energy (~3.37 eV), extensive exciton binding energy (~60 meV) at room temperature, high electronic mobility, high transparency, high thermal conductivity, UV-shielding properties, and excellent photocatalytic activity [2–4]. These properties made ZnO films suitable for optoelectronic applications [5], solar cells [6], gas sensors [7], biosensors [8], photocatalysis [9], and light-emitting devices [10].

Doping ZnO films with different elements, such as group III, transition metals, and rare-earth metals, have variated the physical and chemical properties for various potential applications [11]. Copper (Cu) and nickel (Ni) are considered ideal dopants for ZnO films, since their atomic radius as well as electronic shells are comparable to those of Zn atoms. Therefore, the replacement of Zn by Cu and/or Ni does not lead to vary the lattice constants substantially [12]. Cu-doped ZnO films were used as a NO_2 gas sensor [13], photocatalyst [14], and UV photodetector [15]. Moreover, Ni-doped ZnO films were used in spintronics applications [16] and UV photodetector applications [17]. Moreover, Cu has a deep impurity level, and Ni reveals ferromagnetic nature at room temperature, thus the resultant doping

✉ Qais M. Al-Bataineh
qais.al-bataineh@isas.de

[1] Leibniz Institut für Analytische Wissenschaften-ISAS-e.V., Bunsen-Kirchhoff-Straße 11, 44139 Dortmund, Germany

[2] Department of Physical Sciences, Jordan University of Science & Technology, P.O. Box 3030, Irbid 22110, Jordan

[3] Experimental Physics, TU Dortmund University, 44227 Dortmund, Germany

[4] Nanotechnology Center, The University of Jordan, Amman 11942, Jordan

combination (Cu–Ni)/ZnO is a motivating candidate for attaining innovative properties [18].

A. Ahmad et al. [19] stated that the films prepared by sol–gel synthesis technique using zinc acetate dehydrated, ethanol, and ethanolamine are amorphous zinc hydroxide ($Zn(OH)_2$), while the same film annealing at temperatures above 300 °C was transformed into crystalline zinc oxide (ZnO). However, G. Alvin Shi et al. [20] show that annealing ZnO films near 400 °C have H-containing defects that have the role as shallow donors. Hydrogen, oxygen, and nitrogen impurities are the main causes of defects in TCO films [21]. Hydrogen (H) is a widespread impurity in TCO films which affect optical, optoelectronic, and electrical properties of these films via shallow donors formation, since it forms a covalent bond with neighboring vacant oxygen atoms [22]. Hydrogen impurities in TCO films can be metastable and diffuse through the lattice [23]. The n-type conductivity of metal oxide films such as ZnO can be explained using H impurities that act as shallow donors [20]. The hydrogen impurity forms shallow donor defects in the ZnO structure, affecting the optical, optoelectronic, and electrical properties of ZnO [24–27].

Generally, there are various processes for defect creation in the TCO films during film deposition and post-annealing. Defects creation results in the incorporation of impurities from the ambient during the deposition and/or post-annealing. The defects vary the charge state of the film due to trapping the electrons and holes. The defects interact mutually with each other causing the formation of various forms of defects that diffuse throughout the material.

The main objective of this study is to investigate the hidden impurities and the vacancies-related defects in TCOs by exploring the chemical and structural properties of as-prepared and annealed (Cu–Ni)/ZnO film at 500 °C under 1 atmospheric pressure of air, vacuum, nitrogen, and argon. The chemical and structural properties were investigated relying on using FTIR spectra and XRD pattern. In addition, the effect of these impurities on the optical, optoelectronic, and electrical properties of (Cu–Ni)/ZnO films were investigated by extracting the refractive index, bandgap energy, band structure from the UV–Vis spectra with addition to the electrical conductivity properties from 4-points probe.

2 Experimental set-up and sample preparation

(Cu–Ni)/ZnO in buffer solution form was prepared from (5 wt.% Cu–5 wt.% Ni) co-doped ZnO. An amount of 4.380 g of zinc acetate dehydrated (ZnAc, $Zn(CH_3CO_2)_2.2H_2O$, 183.48 g/mol, purity of 99.5%, Sigma–Aldrich), a 0.219 g of copper acetate (CuAc, $Cu(CH_3COO)_2$, 181.63 g/mol, purity of 99.99%, Sigma-Aldrich) and a 0.219 g of nickel chloride ($NiCl_2$, 129.5994 g/mol, purity of 98%, Sigma-Aldrich) were dissolved in 50 mL absolute ethanol (EtOH, 99.85%, Sigma-Aldrich) under continuous stirring for 1 h at ambient conditions until attaining a milky solution. After that, 1.7 mL of ethanolamine was added as a stabilizer in dropwise addition with continuous stirring until reaching a homogeneous transparent solution. The final solution was centrifuged at 500 rpm for 10 min and then filtered using 0.45 µm filter paper.

The (Cu–Ni)/ZnO films were deposited on fused silica substrates (UV grade, 220 ~ 2500 nm wave band, Double side optical-polished, and refractive index about 1.47) using dip coating technique. Each glass substrate was immersed in (Cu–Ni)/ZnO solution with the selected concentration for 2 h. Later on, coated films were dried using an oven at 110 °C for 15 min and thickness were estimated from cross-sectional SEM image and found to be around 500 nm. As a final step, annealing of the films was conducted at 500 °C for 2 h and cooling down to room temperature at ambient conditions under air, vacuum, nitrogen, and argon atmospheres in the vacuum oven (Electric furnace, SA2-2-12TP) in different individual experiments. The n/p-type was measured using Avometer after heating the films compared with an n-type silicon substrate. Remarkably, the film annealed under nitrogen atmosphere is a p-type, while other films are n-type.

Dissolving ZnAc in EtOH by adding ethanolamine as a stabilizer at ambient conditions produces a clear and homogenous solution of $Zn(OH)_2$ due to reaction between the Zn^{2+} ions revealed from the ZnAc and OH^- ions revealed from the interaction of EtOH with the ethanolamine. Adding CuAc and $NiCl_2$ with calculated concentrations into the starting solution results in $(Cu-Ni)/Zn(OH)_2$ solution [28]. Moreover, the $(Cu-Ni)/Zn(OH)_2$ solution is deposited as a film and transformed into $(Cu-Ni)/ZnO$ film by annealing it at temperatures above 300 °C (Fig. 1). The main process is evaporating the H_2O from the film producing metal oxide film from the metal hydroxide state. However, high temperatures create defects such as hydrogen, oxygen, and nitrogen found in the air. These defects diffuse throughout the film structure via the post-annealing process.

X-ray diffraction (XRD) patterns were obtained at room temperature with XRD instrument (Malvern Panalytical Ltd, Malvern, UK) diffractometer using CuKα radiation (0.1540598 nm) with the incident angels between 30° and 60° with a step of 0.02° and energy resolution of 20%. Fourier transform infrared spectroscopy (FTIR) spectra were obtained with (Bruker Tensor 27) spectrometer in the wavenumber range of 4000–400 cm^{-1}. The UV–Vis spectrophotometer (U–3900H) was used for conducting the UV–Vis spectra in the wavelength range of 250–700 nm. The 2D electrical conductivities at room temperature were obtained with a 4-point probe (Microworld Inc.) equipped with a high-resolution multimeter (Keithley 2450 Sourcemeter).

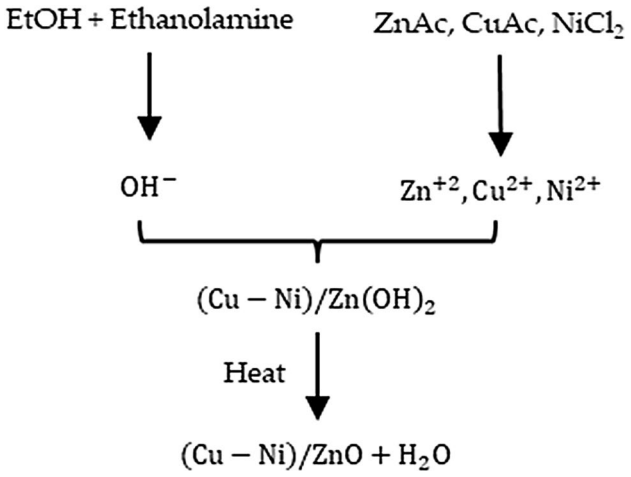

Fig. 1 The schematic diagrams of synthesis method of (Cu – Ni)/ZnO films

3 Results and discussion

The FTIR spectra of (Cu–Ni)/ZnO films exhibit three main bands of stretching Zn–O bonds (420 cm^{-1}) [29], stretching Ni–O bonds (610 cm^{-1}) [30], and stretching Cu–O bonds (670 cm^{-1}) [31] (Fig. 2a). The weak stretching Zn–O bond in the as-deposited film increases of annealing under air and argon atmospheres. While, it disappears in the case of vacuum and nitrogen environments. Remarkably, Ni – O band does not appear in the as-deposited films; and showed up obviously after annealing regardless of the environment. The Cu – O band was shown up more strongly once annealing under nitrogen atmosphere while it is moderated when the annealing is under air, vacuum and argon. The vibrational bands (800 and 1200 cm^{-1}) are associated to the acetate group (carbon, oxygen, and hydrogen), the residuals from the starting materials [32]. H impurities in the metal oxides was determined via the bending O–H bonds (1250–1700 cm^{-1}) and the stretching ZnO : H bonds (~ 3400 cm^{-1}) (Fig. 2a). Annealing (Cu–Ni)/ZnO film at 500 °C in different environments reduces the H impurities [33]. However, the existence of bending O–H bonds and stretching ZnO : H bonds in the annealed films suggests the existence of hydrogen shallow donors in the (Cu–Ni)/ZnO films, that bounds to the oxygen vacancy (H_O) [34]. The fact that(Cu–Ni)/ZnO film annealed under nitrogen environment switched from n-type to p-type explained the appearance of the band at 450 cm^{-1}, this band represents Zn–N bond, this appearance confirms the existence of nitrogen shallow acceptors bounded to zinc vacancy (N_{Zn}) [35]. Generally, H and N impurities related to the oxygen atoms (H_O) and zinc atoms (N_{Zn}) influence the physicochemical properties of metal oxide films [36]. The effect of H-containing defects bounded to the oxygen vacancy (H_O) and N-containing defects bounded to the zinc vacancy (N_{Zn}) on the microstructural properties of (Cu–Ni)/ZnO film, such as crystalline domain size (D) and microstrain ε, were also investigated using Williamson–Hall (WH) method and its modifications.

The XRD diffraction patterns of (Cu–Ni)/ZnO films (Fig. 2b) were indexed by qualitative phase analysis software

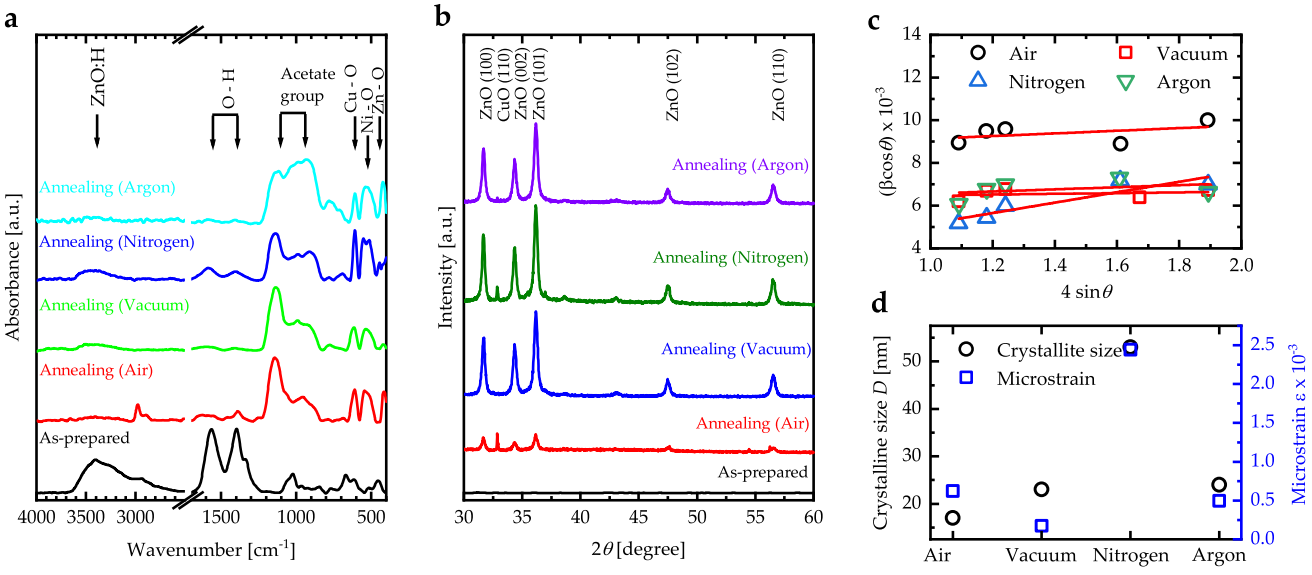

Fig. 2 **a** FTIR spectra, **b** XRD patterns **c** $\beta_{hkl} \cos\theta$ versus $4 \sin\theta$ and **d** D and ε of (Cu–Ni)/ZnO film: as-prepared and annealed at 500 °C under air, vacuum, nitrogen and argon atmospheres

(Qualx2). No diffraction peaks can be observed in as-prepared film indicating that it has amorphous nature. Annealed film under air atmosphere exhibits peaks at 31.68° (ZnO-100), 32.86° (CuO-110), 34.34° (ZnO-002), 36.16° (ZnO-101), 47.60° (ZnO-102), and 56.58° (ZnO-110), that match the standard hexagonal wurtzite ZnO with the space group of P63mc according to the JCPSD card no. (036–1451) [12]. Annealed films under vacuum, nitrogen, and argon atmospheres were led to enhance the crystallinity degree due to reducing the H-containing defects in the films [19].

The crystallinity degree (X_{cryst}%) is defined as the ratio between the integrated area under the diffraction peaks (A_{crys}) to the total area ($A_{crys} + A_{amorph}$) (Table 1) [37, 38]. The film annealed under air atmosphere exhibit a lower crystallinity degree (35%), while those annealed under vacuum or argon exhibited higher degree of crystallinity (66%). This is attributed to the lower H impurities in the (Cu–Ni)/ZnO film, as shown in Fig. 2a. However, the (Cu–Ni)/ZnO film annealed in nitrogen exhibits a lower crystallinity degree than the annealed samples in vacuum or argon due to N impurities, which appears at FTIR band of 450 cm^{-1} (Zn–N bond). The lattice constants of hexagonal structure were calculated using $a = \sqrt{4/3}d_{100}$ and $c = 2d_{002}$ (Table 1), where d_{hkl} is the interplanar distance calculated from Bragg's law ($n\lambda = 2d_{hkl}\sin\theta_{hkl}$) [39, 40].

The crystallite size (D) and microstrain $\langle\varepsilon\rangle$ were calculated using Williamsons–Hall (WH) method [40]. This method states that the total linewidth of the XRD peaks (β_{total}) is composed of a superposition of the particle size linewidth (β_{size}) and microstrain linewidth (β_{strain}), as [41]:

$$\beta_{\text{total}} = \beta_{\text{size}} + \beta_{\text{strain}}. \quad (1)$$

The values of D and $\langle\varepsilon\rangle$ were investigated using the modified WH equation via the uniform deformation model (UDM) [42],

$$\beta_{\text{hkl}}\cos\theta = \frac{k\lambda}{D} + 4\varepsilon\sin\theta. \quad (2)$$

Plotting $\beta_{hkl}\cos\theta$ versus $4\sin\theta$ illustrates the microstrain from the slope, while the crystallite size is calculated using the intercept (Fig. 2c). The average D and $\langle\varepsilon\rangle$ deduced from WH-UDM as explained above are listed in Table 1. The obtained microstrain of the films was the lowest in the case of the annealed film under a vacuum, revealing that film has the lowermost H impurities. In comparison, the higher microstrain was observed in the film annealed under nitrogen atmosphere, suggesting that defects associated with the N have higher impact on the film microstructure comparing to the defects associated with H impurities (Fig. 2d).

The electrical conductivity of metal oxide films depends on many parameters, such as dopant type, dopant concentration, impurities, and crystallinity degree [43]. The as-prepared film has an average conductivity of 2.93 ± 0.2 µS/cm, while the annealed film under air vacuum, nitrogen, and argon atmospheres has average electrical conductivities of 3.77 ± 0.2, 6.71 ± 0.2, 6.48 ± 0.2, and 6.80 ± 0.2 µS/cm, respectively (Fig. 3a). The enhanced electrical conductivity in the annealed films is associated with the enhancement in the degree of crystallinity in addition to the reduction in the H impurities. In spite of that the shallow hydrogen donors bounded to O-vacancies (H_O) are the origin of the n-type of metal oxides [36], the annealed film under nitrogen atmosphere has lower electrical conductivity compared to those annealed films under vacuum and argon due to the existence of shallow nitrogen accepters bounded to Zn-vacancies (N_{Zn}) that are the origins of the p-type of the film. The conductivity mapping of (Cu–Ni)/ZnO film (Fig. 3b–f) shows variation in the surface conductivity due to the growth process and the quality of the transfer process.

The transmittance spectrum of the as-prepared film has a rapid jump in the transmittance from 0 to 90% associated with the increase in the wavelengths only from 300 to 400 nm, while no significant variation is observed in wavelengths between 400 and 700 nm (Fig. 4a). In the annealed films, the transmittance was decreased in the visible region, and the band edge was shifted to the red region (low energy), indicating a decrease in the bandgap energy. In addition, the reflectance was increased in all of the annealed films (Fig. 4b). The bandgap energies (E_g) calculated according to Tauc equation $(\alpha h\nu)^2 = \beta(h\nu - E_g)$, where α is the absorption coefficient ($\alpha = (1/d)\ln((1-R)/T)$) [44], were decreased as the films were annealed (Fig. 4e). Moreover, the minimum occurrence in the obtained bandgap energy was associated with the film annealed under a nitrogen atmosphere, this can be connected to microstrain which has the highest value among all due to the defects induced by the nitrogen as it is presented above.

Table 1 The structural and microstructural parameters of (Cu–Ni)/ZnO film: as-prepared and annealed at 500 °C under air, nitrogen, vacuum, and argon atmospheres determined using XRD

Parameters	Symbol and unit	Air	Vacuum	Nitrogen	Argon
Degree of crystallinity	X_{crys}%	35%	66%	57%	66%
Lattice constants	a[Å]	3.26	3.26	3.26	3.26
	c[Å]	5.23	5.23	5.22	5.22
WH method	D[nm]	17	23	53	24
	$\langle\varepsilon\rangle \times 10^{-4}$	6.2	1.7	24.4	4.9

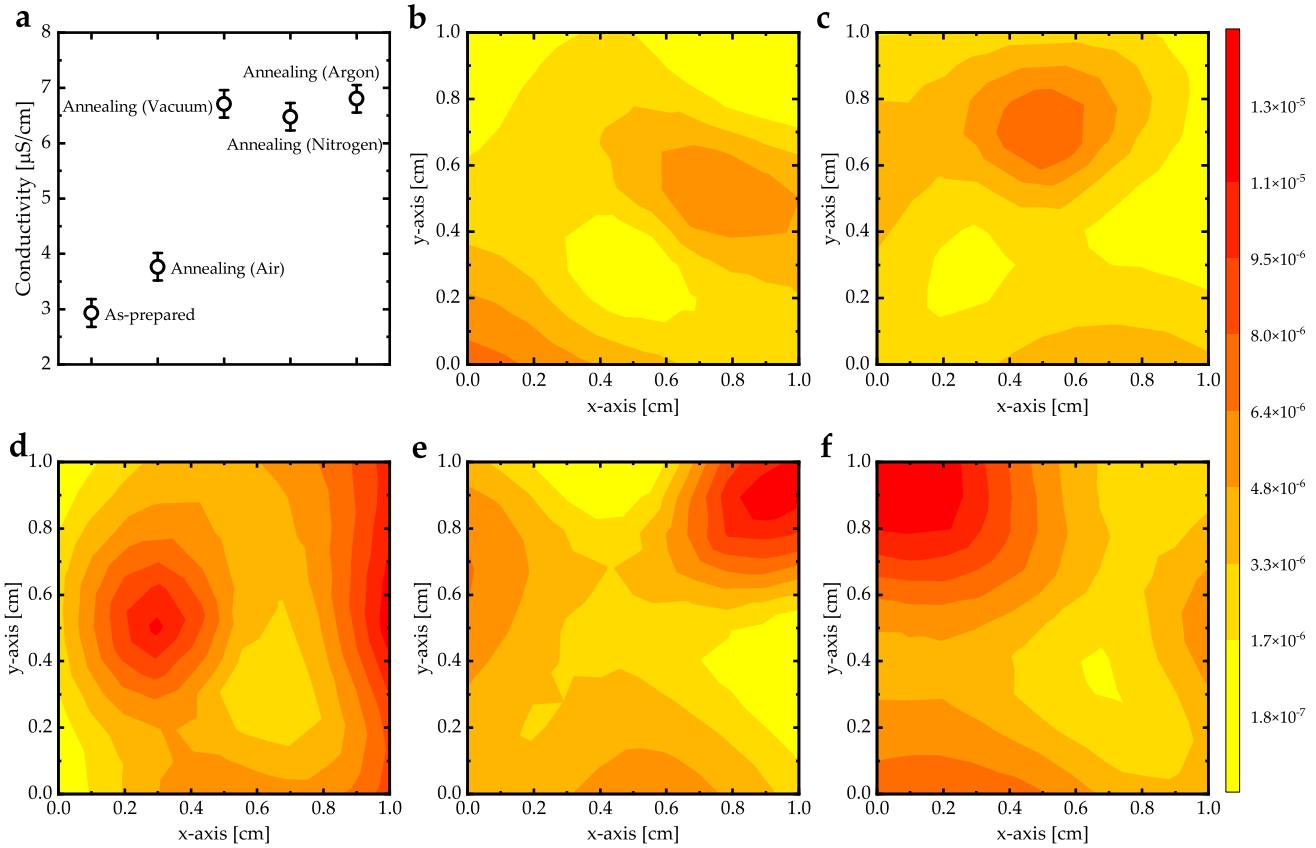

Fig. 3 **a** The average electrical conductivity of (Cu–Ni)/ZnO film: as-prepared and annealed at 500 °C under air, vacuum, nitrogen, and argon atmospheres. The conductivity mapping of the (1 cm × 1 cm) area on the surface of the (Cu–Ni)/ZnO films that is **b** as-prepared, and those annealed under **c** air, **d** vacuum, **e** nitrogen, and **f** argon atmospheres

The H shallow donor and N shallow acceptor defects influencing the valance (VB) and conduction (CB) bands occurred due the disorders were investigated by Urbach energy (E_U) via the equation $\alpha = \alpha_0 \exp(h\nu/E_u)$ [45]. Based on the findings in the literature, the obtained band structure was investigated using ionization and electron affinity energies [46, 47]. The band structure schematic diagram illustrated in Fig. 4f illustrates the shifts in the conduction bands (CB) toward less negative potential as well illustrates the shifts in the valance bands (VB) toward less positive potential in the annealed films compared to the as-prepared one. In addition, the as-prepared (Cu–Ni)/ZnO film has higher Urbach energy, which means higher disorder, indicating a higher existence of H shallow donor defects [19]. However, Urbach energies of the annealed films under vacuum and argon atmospheres have similar and lowest values compare to the others, indicating lowest H shallow donor defects. While, the high Urbach energy value was observed in the annealed film under nitrogen atmosphere connected to the N shallow acceptor defects. Moreover, the average electrical conductivity and bandgap energy for the (Cu–Ni)/ZnO film annealed under vacuum is 6.71 μS/cm and 3.38 eV, respectively. However, the (Cu–Ni)/ZnO film annealed in argon has 6.80 μS/cm and 3.39 eV, average electrical conductivity, and bandgap energy due to the low microstrain from the low H-related defects. Moreover, the average electrical conductivity and bandgap energy for the (Cu − Ni)/ZnO film annealed in nitrogen is 6.48 μS/cm and 3.22 eV, respectively.

The extinction coefficient (k) and refractive index (n) were calculated using $k = \alpha\lambda/4\pi$ and $n = (1 + R/1 - R) + \sqrt{\left(4R/(1-R)^2\right) - k^2}$ [48]. The absolute values of k and n over the wavelength ranges from 250 to 700 nm were observed to be the highest in the case of the film annealed under nitrogen atmosphere (Fig. 4c, d). Which means that the photon penetrates the films with higher decaying or damping (Fig. 4c). The n–spectra of the films (Fig. 4d) exhibits two behaviors, the anomalous type which occurs in the wavelength region ($250 \leq \lambda < 400$ nm), where the incident photon frequency balances the plasma frequency [49]. Besides, the normal behavior occurs in the wavelength region ($400 \leq \lambda < 700$ nm) where

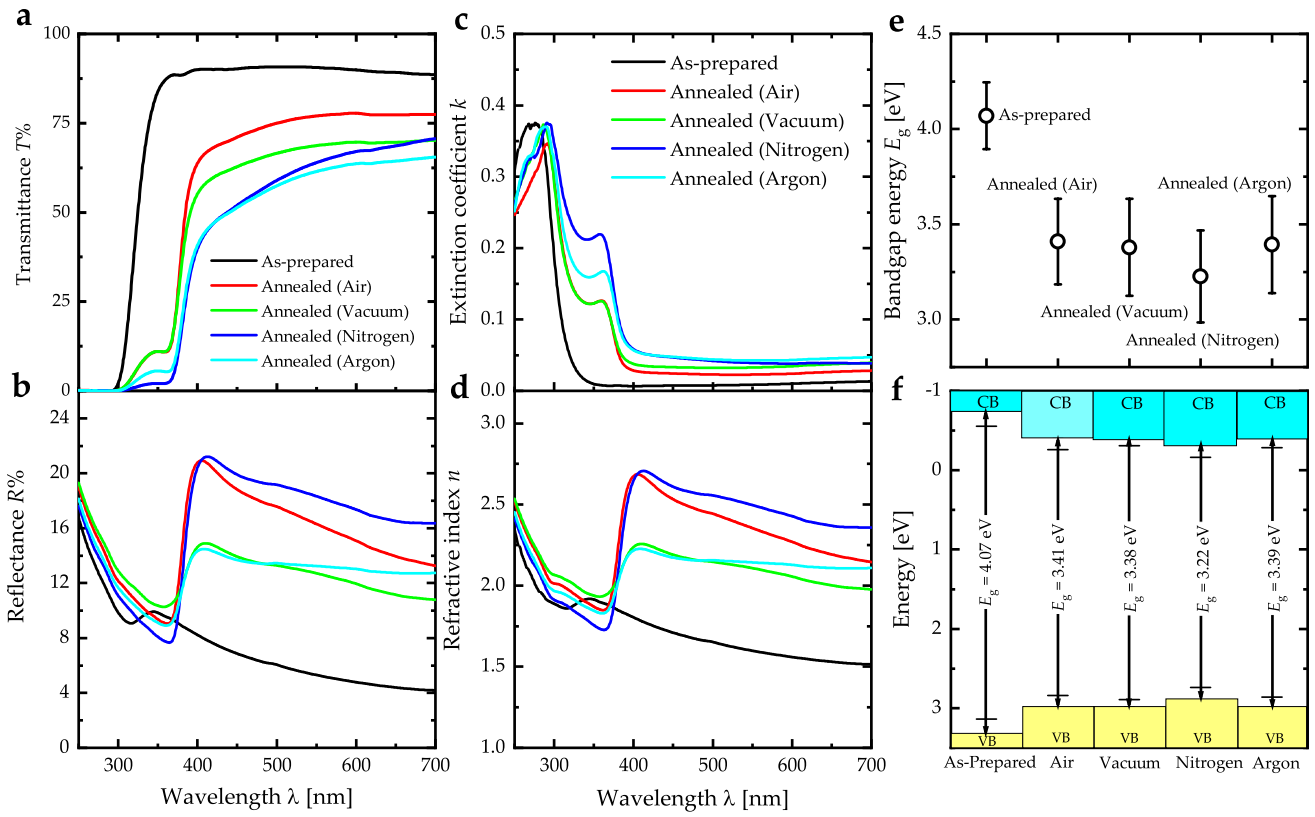

Fig. 4 The **a** transmittance, **b** reflectance, **c** extinction coefficient, and **d** refractive index spectra °C under air, vacuum, nitrogen and argon, **e** The calculated bandgap energies according to Tauc plot and the **f** schematic diagram of the band structure of (Cu–Ni)/ZnO film which are as-prepared and annealed at 500 °C under air, vacuum, nitrogen and argon atmospheres

a normal decrease of the refractive index occurs as the wavelength increases [50].

Generally, there are many processes for defect creation in TCO films during film deposition and post-annealing (Fig. 5a). Defects creation results in the incorporation of impurities from the environment during the deposition and/or post-annealing. These defects change the film charge state due to electron and hole trapping. In addition, defects can react with each other to form different defects, and the final process is defect diffusion [21]. Based on the above results and their interpretation, annealing $(Cu-Ni)/Zn(OH)_2$ film at 500 °C in an air environment produced (Cu – Ni)/ZnO film through many processes (Fig. 5b). The main process that occurs is the H_2O evaporation from the film to transform the film from metal hydroxide to metal oxide. However, high temperatures created defects, hydrogen, and oxygen, in the air components. These defects diffused into the film structure through the post-annealing process. Consequently, these defects could react with each other and/or changes the charge across the film. The annealing of the $(Cu-Ni)/Zn(OH)_2$ film at 500 °C in a vacuum or argon environment produces (Cu – Ni)/ZnO film (Figs. 5c, 4e) was led mainly to evaporate H_2O from the film to produce zinc oxide film from zinc hydroxide, beside reaction between H impurities with oxygen to produce OH^-. Finally, annealing the $(Cu-Ni)/Zn(OH)_2$ film at 500 °C in a nitrogen environment produces (Cu – Ni)/ZnO film with nitrogen defects (Fig. 5d). The main evidence of the existence of N-related defects bound to the zinc vacancy (N_{Zn}) is the transformation from n-type to p-type [35], in addition to evaporating the H_2O from the film. Nitrogen impurities may diffuse into the film, creating N-containing shallow acceptor defects.

4 Conclusions

The (Cu–Ni)/ZnO films were prepared using the sol–gel method and then annealed using an oven at 500 °C for 2 h in different environments (air, vacuum, nitrogen, and argon). The main process occurs through annealing the films is evaporating the H_2O from the films to produce metal oxides from metal hydroxide material. The FTIR spectra confirm the existence of H-related defects bounded to the vacant oxygen (H_O) in the annealed film under air, vacuum, or argon atmospheres that acts as shallow donor defects. In contrast to that, the (Cu–Ni)/ZnO film annealed under a nitrogen

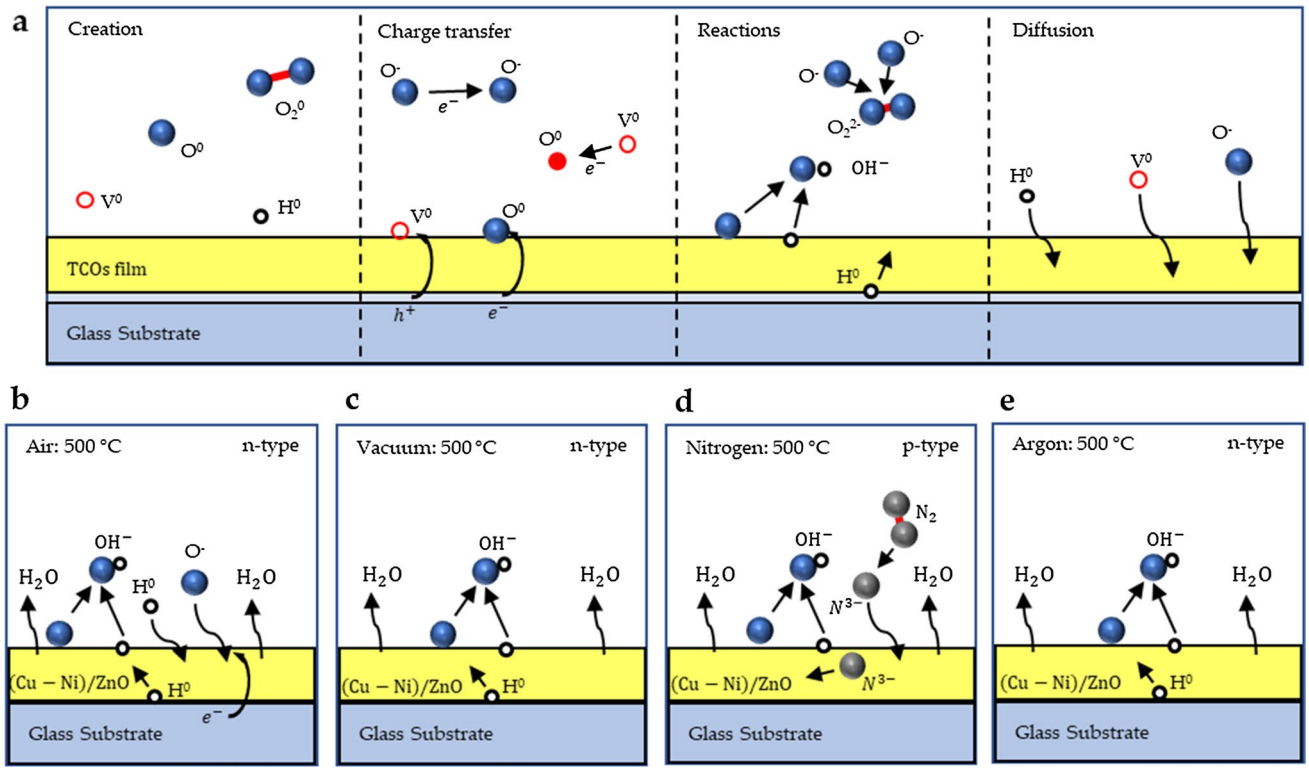

Fig. 5 **a** Processes for defect creation, charge transfer, reactions and diffusion of the defects and charges within and between the TCOs film and the applied atmosphere [21]. Defect creation, possible reactions and diffusions within and between (Cu – Ni)/ZnO film during the annealing under atmospheres of **b** air, **c** vacuum, **d** nitrogen, and **e** argon

atmosphere has developed N-related defects bound to the vacant zinc (N_{Zn}) that acts as shallow acceptor defects. The H-related defects shifts (Cu–Ni)/ZnO film to be an n-type material, while N-related defects shifts the film to be a p-type material. Consequently, the H-related defects were led to a high degree of crystallinity (66%) when films were annealed under vacuum or argon atmospheres. While the film annealed under nitrogen atmosphere exhibits a lower degree of crystallinity due to N-related impurities. Films were annealed under vacuum, nitrogen, and argon atmospheres show higher electrical conductivity compared to the as-prepared one. The bandgap energies of the (Cu–Ni)/ZnO film were decreased as a result of annealing regardless the atmosphere where the annealing was performed; however, the bandgap energy showed the minimum value in the film annealed under a nitrogen atmosphere due to the high microstrain due to the N-related defects. In the film annealed under air atmosphere, the induced defects were led to reduce the degree of crystallinity by 35%. Moreover, the average electrical conductivity and bandgap energy are 3.77 µS/cm and 3.41 eV, respectively.

Acknowledgements The authors would like to acknowledge Jordan University of Science and Technology. We also thank Prof. Mohammad-Ali H. Al-Akhras for helping our members use the biomedical laboratory. Financial Support by the Ministerium für Innovation, Wissenschaft und Forschung des Landes Nordrhein-Westfalen, the Senatsverwaltung für Wirtschaft, Technologie und Forschung des Landes Berlin, and the Bundesministerium für Bildung und Forschung is gratefully acknowledged.

Author contributions QMAl-B: Conceptualization, Methodology, Writing–original draft. AAA: Data acquisition, Writing–review and editing. IAA: Preparation, Data acquisition. AMA: Preparation, Data acquisition. AT: Conceptualization, Supervision, Writing–review and editing.

Funding Open Access funding enabled and organized by Projekt DEAL.

Data availability Not applicable.

Declarations

Conflict of interest The authors declare that they have no known competing financial interests or personal relationships that could have influenced the work reported in this paper.

Consent to participate All authors have participated in this work.

Consent to publish All authors have agreed to publish this work.

References

1. M. Karakawa, T. Sugahara, Y. Hirose, K. Suganuma, Y. Aso, Thin film of amorphous zinc hydroxide semiconductor for optical devices with an energy-efficient beneficial coating by metal organic decomposition process. Sci. Rep. **8**(1), 1–7 (2018)
2. S. Iqbal, N. Ahmad, M. Javed, M.A. Qamar, A. Bahadur, S. Ali, Z. Ahmad, R.M. Irfan, G. Liu, M.B. Akbar, Designing highly potential photocatalytic comprising silver deposited ZnO NPs with sulfurized graphitic carbon nitride (Ag/ZnO/Sg-C3N4) ternary composite. J. Environ. Chem. Eng. **9**(1), 104919 (2021)
3. A. Alsaad, Q.M. Al-Bataineh, A. Ahmad, Z. Albataineh, A. Telfah, Optical band gap and refractive index dispersion parameters of boron-doped ZnO thin films: a novel derived mathematical model from the experimental transmission spectra. Optik **211**, 164641 (2020)
4. A. Alsaad, Q.M. Al-Bataineh, A. Ahmad, I. Jumh, N. Alaqtash, A. Bani-Salameh, Optical properties of transparent PMMA-PS/ZnO NPs polymeric nanocomposite films: UV-shielding applications. Mater. Res. Express **6**(12), 126446 (2020)
5. A. Alsaad, A. Ahmad, I. Qattan, Q.M. Al-Bataineh, Z. Albataineh, Structural, optoelectrical, linear, and nonlinear optical characterizations of dip-synthesized undoped ZnO and group III elements (B, Al, Ga, and In)-doped ZnO thin films. Crystals **10**(4), 252 (2020)
6. S. Bhatt, R. Shukla, C. Pathak, S.K. Pandey, Evaluation of performance constraints and structural optimization of a core-shell ZnO nanorod based eco-friendly perovskite solar cell. Sol. Energy **215**, 473–481 (2021)
7. J. Liu, L. Zhang, J. Fan, B. Zhu, J. Yu, Triethylamine gas sensor based on Pt-functionalized hierarchical ZnO microspheres. Sens. Actuators B Chem. **331**, 129425 (2021)
8. G.S. Mei, P.S. Menon, G. Hegde, ZnO for performance enhancement of surface plasmon resonance biosensor: a review. Mater. Res. Express **7**(1), 012003 (2020)
9. B. Albiss, M. Abu-Dalo, Photocatalytic degradation of methylene blue using zinc oxide nanorods grown on activated carbon fibers. Sustainability **13**(9), 4729 (2021)
10. E. Moyen, J.H. Kim, J. Kim, J. Jang, ZnO nanoparticles for quantum-dot-based light-emitting diodes. ACS Appl. Nano Mater. **3**(6), 5203–5211 (2020)
11. E. Asikuzun, O. Ozturk, L. Arda, C. Terzioglu, Preparation, growth and characterization of nonvacuum Cu-doped ZnO thin films. J. Mol. Struct. **1165**, 1–7 (2018)
12. A. Ahmad, A. Migdadi, A. Alsaad, Q.M. Al-Bataineh, A. Telfah, Optical, structural, and morphological characterizations of synthesized (Cd–Ni) co-doped ZnO thin films. Appl. Phys. A **127**(12), 1–12 (2021)
13. V. Patil, S. Vanalakar, N. Tarwal, A. Patil, T. Dongale, J. Kim, P. Patil, Construction of Cu doped ZnO nanorods by chemical method for Low temperature detection of NO2 gas. Sens. Actuators A **299**, 111611 (2019)
14. W. Vallejo, A. Cantillo, B. Salazar, C. Diaz-Uribe, W. Ramos, E. Romero, M. Hurtado, Comparative study of ZnO thin films doped with transition metals (Cu and Co) for methylene blue photodegradation under visible irradiation. Catalysts **10**(5), 528 (2020)
15. I. Ben Elkamel, N. Hamdaoui, A. Mezni, R. Ajjel, L. Beji, Synthesis and characterization of Cu doped ZnO nanoparticles for stable and fast response UV photodetector at low noise current. J. Mater. Sci. **30**(10), 9444–9454 (2019)
16. S. Ghosh, C. Choubey, A. Sil, Photocatalytic response of Fe Co, Ni doped ZnO based diluted magnetic semiconductors for spintronics applications. Superlattices Microstruct. **125**, 271–280 (2019)
17. Y.-L. Chu, L.-W. Ji, Y.-J. Hsiao, H.-Y. Lu, S.-J. Young, I.-T. Tang, T.-T. Chu, X.-J. Chen, Fabrication and characterization of Ni-Doped ZnO nanorod arrays for UV photodetector application. J. Electrochem. Soc. **167**(6), 067506 (2020)
18. A. Guler, L. Arda, N. Dogan, C. Boyraz, E. Ozugurlu, The annealing effect on microstructure and ESR properties of (Cu/Ni) co-doped ZnO nanoparticles. Ceram. Int. **45**(2), 1737–1745 (2019)
19. A.A. Ahmad, Q.M. Al-Bataineh, I.A. Aljarrah, A.D. Telfah, Electrochemical degradation of methyl red in zinc hydroxide and zinc oxide thin films, physical and chemical activation. Mater. Chem. Phys. **280**, 125793 (2022)
20. G.A. Shi, M. Saboktakin, M. Stavola, S. Pearton, "Hidden hydrogen" in as-grown ZnO. Appl. Phys. Lett. **85**(23), 5601–5603 (2004)
21. A. Shluger, Defects in oxides in electronic devices, in *Handbook of materials modeling: applications: current and emerging materials*. (Springer nature, Berlin, 2020), pp.1013–1034
22. D. Bastin, E. Lavrov, J. Weber, Metastable state of the V Zn H 2 defect in ZnO. Phys. Rev. B **83**(19), 195210 (2011)
23. H. Li, J. Robertson, Behaviour of hydrogen in wide band gap oxides. J. Appl. Phys. **115**(20), 203708 (2014)
24. K. Shimomura, K. Nishiyama, R. Kadono, Electronic structure of the muonium center as a shallow donor in ZnO. Phys. Rev. Lett. **89**(25), 255505 (2002)
25. D.M. Hofmann, A. Hofstaetter, F. Leiter, H. Zhou, F. Henecker, B.K. Meyer, S.B. Orlinskii, J. Schmidt, P.G. Baranov, Hydrogen: a relevant shallow donor in zinc oxide. Phys. Rev. Lett. **88**(4), 045504 (2002)
26. B.K. Meyer, H. Alves, D. Hofmann, W. Kriegseis, D. Forster, F. Bertram, J. Christen, A. Hoffmann, M. Straßburg, M. Dworzak, Bound exciton and donor–acceptor pair recombinations in ZnO. Physica status solidi (b) **241**(2), 231–260 (2004)
27. F. Herklotz, E. Lavrov, V. Kolkovsky, J. Weber, M. Stavola, Charge states of a hydrogen defect with a local vibrational mode at 3326 cm−1 in ZnO. Phys. Rev. B **82**(11), 115206 (2010)
28. A.H. Adl, P. Kar, S. Farsinezhad, H. Sharma, K. Shankar, Effect of sol stabilizer on the structure and electronic properties of solution-processed ZnO thin films. RSC Adv. **5**(106), 87007–87018 (2015)
29. J.-L. Chen, N. Devi, N. Li, D.-J. Fu, X.-W. Ke, Synthesis of Pr-doped ZnO nanoparticles: their structural, optical, and photocatalytic properties. Chin. Phys. B **27**(8), 086102 (2018)
30. A. Abd, R. Ali, A. Hussein, Fabrication and characterization of nickel oxide nanoparticles/silicon heterojunction. J Multidiscip Eng Sci Stud **2**, 434–440 (2016)
31. N. Mukwevho, E. Fosso-Kankeu, F. Waanders, N. Kumar, S.S. Ray, X. YangkouMbianda, Photocatalytic activity of Gd2O2CO3 ZnO CuO nanocomposite used for the degradation of phenanthrene. SN Appl. Sci. **1**(1), 1–11 (2019)
32. N. Akbar, Z. Aslam, R. Siddiqui, M.R. Shah, N.A. Khan, Zinc oxide nanoparticles conjugated with clinically-approved medicines as potential antibacterial molecules. AMB Express **11**(1), 1–16 (2021)
33. A.A. Ahmad, Q.M. Al-Bataineh, I.A. Aljarrah, A.D. Telfah, Electrochemical degradation of methyl red in zinc hydroxide and zinc oxide thin films, physical and chemical activation. Mater. Chem. Phys. **280**, 12579 (2022)

34. A. Janotti, C.G. Van de Walle, Hydrogen multicentre bonds. Nat. Mater. **6**(1), 44–47 (2007)
35. Z. Fu-Jian, M. Hong-Lei, L. Wei, D. Wei, Z. Xi-Jian, X. Hong-Di, M. Jin, J. Feng, X. Cheng-Shan, Z. Hui-Zhao, Thermal decomposition behaviour of Zn3N2 powder. Chin. Phys. Lett. **22**(4), 907 (2005)
36. T. Cossuet, F. Donatini, A.M. Lord, E. Appert, J. Pernot, V. Consonni, Polarity-dependent high electrical conductivity of ZnO nanorods and its relation to hydrogen. J. Phys. Chem. C **122**(39), 22767–22775 (2018)
37. A.A. Akl, I. El Radaf, A.S. Hassanien, An extensive comparative study for microstructural properties and crystal imperfections of novel sprayed Cu3SbSe3 nanoparticle-thin films of different thicknesses. Optik **227**, 165837 (2021)
38. A. Sa, A.A. Akl, A.S. Hassanien, Effective role of Rb doping in controlling crystallization, crystal imperfections, microstructural, and morphological features of ZnO-NPs synthesized by Sol-Gel way. CrystEngComm **24**, 4661–4678 (2022)
39. A. Ahmad, A. Alsaad, Q. Al-Bataineh, A. Bani-Salameh, H. Al-Khateeb, M. Al-Naafa, Optical and structural characterization of dip synthesized Al-B Co-doped ZnO seeded platforms for ZnO nanostructures. Jordan J. Phys. **10**(1), 33–48 (2017)
40. A.A. Akl, A.S. Hassanien, Comparative microstructural studies using different methods: effect of Cd-addition on crystallography, microstructural properties, and crystal imperfections of annealed nano-structural thin CdxZn1-xSe films. Physica B **620**, 413267 (2021)
41. A. Hassanien, A.A. Akl, A. Sáaedi, Synthesis, crystallography, microstructure, crystal defects, and morphology of Bi x Zn 1–x O nanoparticles prepared by sol–gel technique. CrystEngComm **20**(12), 1716–1730 (2018)
42. A.A. Akl, I. El Radaf, A.S. Hassanien, Intensive comparative study using X-Ray diffraction for investigating microstructural parameters and crystal defects of the novel nanostructural ZnGa2S4 thin films. Superlattices Microstruct. **143**, 106544 (2020)
43. Q.M. Al-Bataineh, I.A. Aljarrah, A.A. Ahmad, A.M. Alsaad, A. Telfah, Investigation of the doping mechanism and electron transition bands of PEO/KMnO4 complex composite films. J. Mater. Sci. **33**, 1–12 (2022)
44. A.S. Hassanien, H.R. Alamri, I. El Radaf, Impact of film thickness on optical properties and optoelectrical parameters of novel CuGaGeSe4 thin films synthesized by electron beam deposition. Opt. Quant. Electron. **52**(7), 1–18 (2020)
45. A.S. Hassanien, I. Sharma, K.A. Aly, Linear and nonlinear optical studies of thermally evaporated chalcogenide a-Pb-Se-Ge thin films. Physica B **613**, 412985 (2021)
46. A. Hassanien, A.A.J.S. Akl, Microstructures, Effect of Se addition on optical and electrical properties of chalcogenide CdSSe thin films. Superlattices Microstruct. **89**, 153–169 (2016)
47. Q.M. Al-Bataineh, A.A. Ahmad, A. Alsaad, A.D.J.H. Telfah, Optical characterizations of PMMA/metal oxide nanoparticles thin films: bandgap engineering using a novel derived model. Heliyon **7**(1), e05952 (2021)
48. A. Ahmad, A. Alsaad, Q. Al-Bataineh, M. Al-Naafa, Optical and structural investigations of dip-synthesized boron-doped ZnO-seeded platforms for ZnO nanostructures. Appl. Phys. A **124**(6), 458 (2018)
49. A.A. Ahmad, M.H. Khazaleh, A.M. Alsaad, Q.M. Al-Bataineh, A.D. Telfah, Characterization of As-prepared PVA-PEO/ZnO-Al2O3-NPs hybrid nanocomposite thin films. Polym. Bullet. **79**, 9881–9905 (2021)
50. M. Telfah, A. Ahmad, A. Alsaad, Q.M. Al-Bataineh, A. Telfah, Doping mechanism and optical properties of as-prepared polyvinyl chloride (PVC) doped by iodine thin films. Polym. Bullet. (2022). https://doi.org/10.1007/s00289-022-04082-9